Chapter 3

Coupled Solid-Liquid Dynamics

In the previous chapter the motion of a liquid in a stationary container has been discussed; the motion of the container was not affected by the sloshing liquid. In this chapter the coupling of the solid-body motion and the motion of the liquid is studied.

3.1 Introduction

Usually, in practical applications, the motion of a container carrying liquid is not prescribed, but follows from an interaction with the liquid motion: the sloshing liquid induces a force and torque on the container, which, as a consequence, starts to accelerate. In return, this container motion influences the liquid motion, and so forth (see [15, 22, 64] for terrestrial examples of solid-liquid interaction).

The coupling of the solid-body dynamics and the liquid dynamics is the focus of this chapter. The coupling consists of two parts. The influence of the solid-body motion on the liquid dynamics is modelled as a virtual body force in the Navier-Stokes equations (section 3.2). The model for the solid-body dynamics is explained in section 3.3. The governing equations for the solid-body dynamics, influenced by the motion of the liquid, are studied in section 3.3.1. These equations are written in such a form that the discretisation results in a stable integration scheme for arbitrary liquid/solid mass ratios. The stability of the integration scheme is exemplified with a simple mass-spring model in section 3.3.2. The actual discretisation of the equations for the solid-body dynamics and the solution of the discretised equations is discussed in section 3.3.3 and section 3.3.4 respectively. In section 3.4 results are presented.

3.2 Liquid Dynamics

3.2.1 Virtual Body Force

In the first step towards the coupling of the solid-body dynamics and the liquid dynamics, it is explained how the motion of the liquid, influenced by the motion of the solid body in which the liquid is contained, is modelled. Hereto, the liquid velocity is considered in two reference frames: the velocity $\boldsymbol{v}$ of a liquid particle with respect to an inertial reference frame $\mathcal{O}'x'y'z'$ and the velocity $\boldsymbol{u}$ of the same liquid particle with respect to a moving

reference frame $\mathcal{O}xyz$. The relation between $\boldsymbol{u}$ and $\boldsymbol{v}$ is given by

$$\frac{D\boldsymbol{v}}{Dt} = \dot{\boldsymbol{q}} + \dot{\boldsymbol{\omega}} \times \boldsymbol{r} + \boldsymbol{\omega} \times (\boldsymbol{\omega} \times \boldsymbol{r}) + \frac{D\boldsymbol{u}}{Dt} + 2\boldsymbol{\omega} \times \boldsymbol{u}, \tag{3.1}$$

where $\dot{\boldsymbol{q}} = d\boldsymbol{q}/dt + \boldsymbol{\omega} \times \boldsymbol{q}$ is the acceleration of the moving origin $\mathcal{O}$ with respect to the origin $\mathcal{O}'$ of the inertial reference frame, $\dot{\boldsymbol{\omega}} = d\boldsymbol{\omega}/dt + \boldsymbol{\omega} \times \boldsymbol{\omega} = d\boldsymbol{\omega}/dt$ is the angular acceleration of the moving reference frame, $\boldsymbol{\omega}$ is the angular velocity of the moving reference frame $\mathcal{O}xyz$, and $\boldsymbol{r}$ is the position of the liquid particle in $\mathcal{O}xyz$. The third and fifth term in the right-hand side of equation (3.1) represent the centrifugal and Coriolis acceleration respectively (see also [26]). Now, the Navier-Stokes equations read

$$\frac{D\boldsymbol{v}}{Dt} = -\frac{1}{\rho}\left(\nabla p - (\nabla \cdot \mu\nabla)\,\boldsymbol{u}\right) + \boldsymbol{F}, \tag{3.2}$$

or, equivalently, using equation (3.1)

$$\frac{D\boldsymbol{u}}{Dt} = -\frac{1}{\rho}\left(\nabla p - (\nabla \cdot \mu\nabla)\,\boldsymbol{u}\right) + \boldsymbol{F} + \boldsymbol{f}, \tag{3.3}$$

where

$$\boldsymbol{f} = -\dot{\boldsymbol{q}} - \dot{\boldsymbol{\omega}} \times \boldsymbol{r} - \boldsymbol{\omega} \times (\boldsymbol{\omega} \times \boldsymbol{r}) - 2\boldsymbol{\omega} \times \boldsymbol{u}. \tag{3.4}$$

Equation (3.3) has a form similar to equation (2.2), meaning that in the numerical model for the liquid dynamics only little change is required. Using Newton's third law, the extra term $\boldsymbol{f}$ in equation (3.3) can be seen as an acceleration due to a virtual body force: instead of actually moving the solid body in the numerical model, the fluid is subjected to an acceleration (equal in magnitude and opposite in sign) to account for the solid-body motion.

3.2.2 Example

For demonstrating the concept of a virtual body force for incorporating solid-body motion in the model for the liquid dynamics, an exemplifying simulation is studied in this section.

Consider a rectangular container with coordinates $[-10, 10] \times [-2, 2]$ in which a square of fluid with coordinates $[4, 6] \times [-1, 1]$ is placed. The fluid is not subjected to gravitational or capillary forces. The container is subjected to a sinusoidal motion; say that the horizontal component of the geometric centre at time t is located at $-5\cos(2\pi t) + 5$ (the vertical component is kept equal to zero). In this case, the fluid experiences no force (since it does not come in contact with the container) and therefore should stay at its initial position. However, in the numerical model not the solid body but the fluid is moved, whence the horizontal component of the centre of mass of the fluid should follow the path given by $5\cos(2\pi t)$ (with respect to the moving reference frame). The results in figure 3.1 confirm this. In this figure the path of the centre of mass of the fluid (with respect to the moving reference frame) is plotted as a function of time (dashed line). When the path of the container is added to this graph, the solid line appears, indicating that the fluid is at rest with respect to an inertial reference frame.

This simulation has been repeated in all Cartesian directions. Furthermore, similar simulations have been performed for validating the virtual body force in the case of

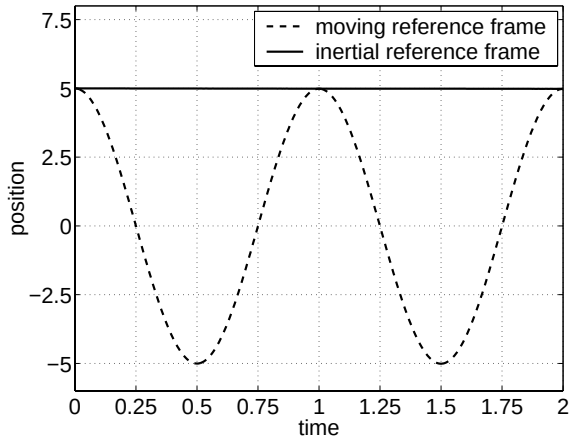

Figure 3.1: *Path of the centre of mass (horizontal component) of the fluid with respect to a moving reference frame and with respect to an inertial reference frame.*

angular motion. Results from these simulations are identical to figure 3.1, from which it is concluded that the concept of a virtual body force works properly and is correctly implemented (see also [78]).

3.3 Solid-Body Dynamics

3.3.1 Governing Equations

The model for the solid-body motion consists of an equation for linear momentum

$$m_s\dot{\boldsymbol{q}} + \dot{\boldsymbol{\omega}} \times m_s\overline{\boldsymbol{r}}_s + \boldsymbol{\omega} \times (\boldsymbol{\omega} \times m_s\overline{\boldsymbol{r}}_s) = \boldsymbol{\mathcal{F}} + m_s\boldsymbol{F}, \tag{3.5a}$$

and an equation for angular momentum

$$m_s\overline{\boldsymbol{r}}_s \times \dot{\boldsymbol{q}} + \boldsymbol{I}_s\dot{\boldsymbol{\omega}} + \boldsymbol{\omega} \times \boldsymbol{I}_s\boldsymbol{\omega} = \boldsymbol{\mathcal{T}} + m_s\overline{\boldsymbol{r}}_s \times \boldsymbol{F}. \tag{3.5b}$$

In these equations $\boldsymbol{q}$ and $\boldsymbol{\omega}$ are the unknown variables, representing the linear and angular velocity of the solid body respectively. The mass of the solid body is denoted by m_s. Further, $\boldsymbol{I}_s$ is the moment-of-inertia tensor and $\overline{\boldsymbol{r}}_s$ is the centre of mass of the solid body. Note that the latter two quantities are relative to the moving reference frame. The last terms in (3.5a) and (3.5b) represent the force and torque due to, for example, gravity. Finally, $\boldsymbol{\mathcal{F}}$ and $\boldsymbol{\mathcal{T}}$ are respectively the force and torque that the fluid, via pressure (normal stress) and viscous effects (tangential stress), exerts on the boundary of the solid body, *i.e.*

$$\boldsymbol{\mathcal{F}} = \oint_{\partial V} (p\boldsymbol{I}_3 - \mu\nabla\boldsymbol{u}) \cdot \boldsymbol{n}\, dS,$$

$$\boldsymbol{\mathcal{T}} = \oint_{\partial V} (\boldsymbol{r} \times (p\boldsymbol{I}_3 - \mu\nabla\boldsymbol{u})) \cdot \boldsymbol{n}\, dS.$$

Here, $\boldsymbol{I}_3$ is the 3×3 identity matrix and $\boldsymbol{n}$ the outward-pointing normal on the boundary ∂V of the total volume V of the solid body. Using the divergence theorem, these integrals can be written as integrals over the volume V (see also [94]):

$$\boldsymbol{\mathcal{F}} = \int_V \nabla p - (\nabla \cdot \mu \nabla)\, \boldsymbol{u}\, dV = -\int_V \rho \left(\frac{D\boldsymbol{v}}{Dt} - \boldsymbol{F} \right) dV,$$

$$\boldsymbol{\mathcal{T}} = \int_V \boldsymbol{r} \times (\nabla p - (\nabla \cdot \mu \nabla)\, \boldsymbol{u})\, dV = -\int_V \rho \boldsymbol{r} \times \left(\frac{D\boldsymbol{v}}{Dt} - \boldsymbol{F} \right) dV.$$

In the last step the Navier-Stokes equations (3.2) were used. Note that the integration in the previous equations is not only over the liquid volume, but also over the void. In the void the density is set to zero, such that the void region does not contribute to the integral.

Direct discretisation of the system (3.5) would result in a method that is not stable for arbitrary liquid/solid mass ratios (this is demonstrated in section 3.4.1 and exemplified with a simple mass-spring model in section 3.3.2). Therefore, the system for the solid-body dynamics is rewritten first. Consider the first term on the right-hand side of equation (3.5a)

$$\boldsymbol{\mathcal{F}} = -\int_V \rho \left(\frac{D\boldsymbol{v}}{Dt} - \boldsymbol{F} \right) dV.$$

Using relation (3.1) for the liquid velocity $\boldsymbol{v}$ with respect to an inertial reference frame and the liquid velocity $\boldsymbol{u}$ with respect to a moving reference frame, the force $\boldsymbol{\mathcal{F}}$ is rewritten as

$$\boldsymbol{\mathcal{F}} = -\int_V \rho \left(\dot{\boldsymbol{q}} + \dot{\boldsymbol{\omega}} \times \boldsymbol{r} + \boldsymbol{\omega} \times (\boldsymbol{\omega} \times \boldsymbol{r}) + \frac{D\boldsymbol{u}}{Dt} + 2\boldsymbol{\omega} \times \boldsymbol{u} - \boldsymbol{F} \right) dV.$$

Since the linear velocity $\boldsymbol{q}$ and the angular velocity $\boldsymbol{\omega}$ of the solid body are constant over the volume V, this is equal to

$$\begin{aligned} \boldsymbol{\mathcal{F}} = &- \dot{\boldsymbol{q}} \int_V \rho\, dV - \dot{\boldsymbol{\omega}} \times \int_V \rho \boldsymbol{r}\, dV - \boldsymbol{\omega} \times \left(\boldsymbol{\omega} \times \int_V \rho \boldsymbol{r}\, dV \right) \\ &- \int_V \rho \left(\frac{D\boldsymbol{u}}{Dt} + 2\boldsymbol{\omega} \times \boldsymbol{u} - \boldsymbol{F} \right) dV. \end{aligned}$$

In short, denoting the liquid mass with m_l and the centre of mass of the liquid with $\overline{\boldsymbol{r}}_l$ (with respect to the moving reference frame), this can be written as

$$\boldsymbol{\mathcal{F}} = -m_l \dot{\boldsymbol{q}} - \dot{\boldsymbol{\omega}} \times m_l \overline{\boldsymbol{r}}_l - \boldsymbol{\omega} \times (\boldsymbol{\omega} \times m_l \overline{\boldsymbol{r}}_l) - \int_V \rho \left(\frac{D\boldsymbol{u}}{Dt} + 2\boldsymbol{\omega} \times \boldsymbol{u} - \boldsymbol{F} \right) dV.$$

Similarly, the torque $\boldsymbol{\mathcal{T}}$ on the right-hand side of equation (3.5b) can be rewritten, which results in

$$\boldsymbol{\mathcal{T}} = -m_l \overline{\boldsymbol{r}}_l \times \dot{\boldsymbol{q}} - \boldsymbol{I}_l \dot{\boldsymbol{\omega}} - \boldsymbol{\omega} \times \boldsymbol{I}_l \boldsymbol{\omega} - \int_V \rho \boldsymbol{r} \times \left(\frac{D\boldsymbol{u}}{Dt} + 2\boldsymbol{\omega} \times \boldsymbol{u} - \boldsymbol{F} \right) dV,$$

where $\boldsymbol{I}_l$ is the moment-of-inertia tensor of the liquid (with respect to the moving reference frame). Substituting these expressions for $\boldsymbol{\mathcal{F}}$ and $\boldsymbol{\mathcal{T}}$ in the system (3.5) and rearranging terms gives an alternative form of the model for the solid-body dynamics, namely

$$m\dot{\boldsymbol{q}} + \dot{\boldsymbol{\omega}} \times m\overline{\boldsymbol{r}} + \boldsymbol{\omega} \times (\boldsymbol{\omega} \times m\overline{\boldsymbol{r}}) = -\int_V \rho \left(\frac{D\boldsymbol{u}}{Dt} + 2\boldsymbol{\omega} \times \boldsymbol{u} - \boldsymbol{F} \right) dV + m_s \boldsymbol{F}, \tag{3.8a}$$

$$m\overline{\boldsymbol{r}} \times \dot{\boldsymbol{q}} + \boldsymbol{I}\dot{\boldsymbol{\omega}} + \boldsymbol{\omega} \times \boldsymbol{I}\boldsymbol{\omega} = -\int_V \rho \boldsymbol{r} \times \left(\frac{D\boldsymbol{u}}{Dt} + 2\boldsymbol{\omega} \times \boldsymbol{u} - \boldsymbol{F} \right) dV + m_s \overline{\boldsymbol{r}}_s \times \boldsymbol{F}. \tag{3.8b}$$

In these equations $m = m_s + m_l$ is the total mass, $\boldsymbol{I} = \boldsymbol{I}_s + \boldsymbol{I}_l$ the moment-of-inertia tensor of the coupled system, and $\overline{\boldsymbol{r}} = (m_s \overline{\boldsymbol{r}}_s + m_l \overline{\boldsymbol{r}}_l)/m$ the centre of mass of the coupled system. Note that the sloshing liquid makes the latter two quantities time dependent.

An important difference between the systems (3.5) and (3.8) is the distribution of the solid-body mass and the liquid mass over the left-hand side and right-hand side of the equations. In the former system the left-hand side contains the mass of the solid body, while on the other side the mass of the liquid, which is moving in the inertial reference frame, appears. Intuitively, one can see that solving this system iteratively, where the left-hand side and right-hand side are evaluated at the new and old time level respectively, can become unstable if the liquid mass is too large with respect to the mass of the solid body. In the latter system the total mass of the coupled system, *i.e.* the sum of the solid-body mass and the liquid mass, appears on the left-hand side. Now, the right-hand side contains the liquid mass in the moving reference frame. In this case, solving this system iteratively can be done in a stable manner since the liquid mass is always smaller than the total mass of the coupled system.

Before discussing the discretisation of (3.8), the stability of a mass-spring model, that exhibits similar characteristics as the model that has been discussed in this section, will be analysed.

3.3.2 Mass-Spring Model

Numerical Instability

Consider, as shown in figure 3.2, a system of two coupled masses m_s and m_l. For consistency these masses are referred to as the solid-body mass and the liquid mass respectively, although, in the present section, the liquid mass is a solid as well. The masses are connected by a spring, having a spring constant k and length ℓ. The system is partitioned

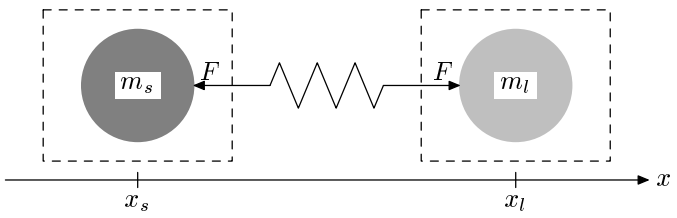

Figure 3.2: *Partitioning of mass-spring system (possibly unstable coupling).*

as indicated by the dashed rectangles, such that the solid-body mass is on one side and the liquid mass is on the other side. This partitioning corresponds to system (3.5). For the mechanical system in figure 3.2 the equations of motion read

$$m_s \ddot{x}_s = -F, \tag{3.9a}$$
$$m_l \ddot{x}_l = F, \tag{3.9b}$$
$$k\,(x_l - x_s - \ell) = -F. \tag{3.9c}$$

Although an analytical solution of this system is easily found, in this section the equations are solved iteratively for demonstrating the stability of the iteration process. Assuming that the solid body moves in reaction to the liquid forces, the left-hand side of equation (3.9a) is discretised at the new iteration level $n+1$, while the right-hand side is evaluated at the old level n. In the remaining two equations (3.9b) and (3.9c) all variables are evaluated at level $n+1$, which results in the following discrete version of system (3.9)

$$m_s \ddot{x}_s^{(n+1)} = -F^{(n)}, \tag{3.10a}$$
$$m_l \ddot{x}_l^{(n+1)} - F^{(n+1)} = 0, \tag{3.10b}$$
$$x_l^{(n+1)} + \frac{1}{k} F^{(n+1)} = x_s^{(n+1)} + \ell, \tag{3.10c}$$

where the iteration level is denoted with a superscript. From this system the variables x_s and x_l can be eliminated by differentiating (3.10c) twice with respect to time and then substituting equations (3.10a) and (3.10b) in this equation. After rearranging terms this gives

$$\frac{m_l}{k} \ddot{F}^{(n+1)} + F^{(n+1)} = -\frac{m_l}{m_s} F^{(n)}. \tag{3.11}$$

In the case of an infinitely stiff coupling, *i.e.* $k = \infty$, this iterative process is stable if and only if $m_l/m_s < 1$; the liquid mass must not exceed the mass of the solid body.

Obviously, in this simple model, if $m_l/m_s > 1$, the role of the liquid and solid body can be interchanged to make the iterative process stable. However, if the models for the solid-body dynamics and the liquid dynamics are very different, as is the case in the rest of this thesis, this solution is not an option.

Stable Numerical Coupling

Of course, the stability problems encountered above can be overcome by solving the system (3.9) simultaneously. However, as pointed out before, this would be very inconvenient since in practice the models for the solid-body dynamics and liquid dynamics are solved with very different algorithms. Therefore, inspired by the quasi-simultaneous method developed for aerodynamical flow [12, 77], the dynamics of the solid body and the liquid are partitioned in such a way that the numerical method is stable for arbitrary liquid/solid mass ratios. This is achieved by adding a term $m_l \ddot{x}_s^{(n+1)}$ to the left-hand side of equation (3.10a). The same term is added to the right-hand side of this equation, but here with iteration index (n). Thus, equation (3.10a) is changed to

$$(m_s + m_l)\, \ddot{x}_s^{(n+1)} = -F^{(n)} + m_l \ddot{x}_s^{(n)}. \tag{3.12}$$

This equation is combined with equations (3.10b) and (3.10c), which, after eliminating x_s and x_l, results in

$$\frac{m_l}{k}\ddot{F}^{(n+1)} + F^{(n+1)} = \frac{m_l}{m_s + m_l}\frac{m_l}{k}\ddot{F}^{(n)}. \tag{3.13}$$

Compared to equation (3.11) the right-hand side has changed. The important difference is the factor $m_l/(m_s + m_l)$, which is always less than one, on the right-hand side of equation (3.13) instead of a factor m_l/m_s in (3.11).

Graphically, the partitioning of the coupled system that is shown in equation (3.12) can be illustrated as in figure 3.3. The idea is that a "frozen" state of the liquid is treated

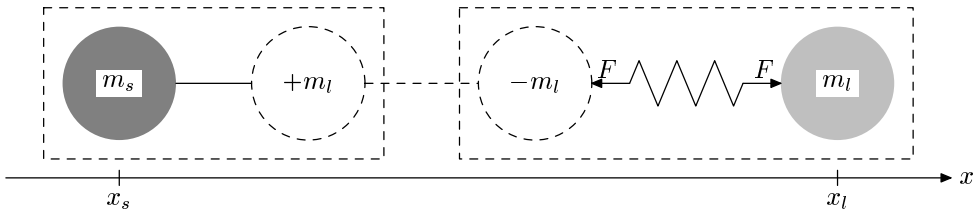

Figure 3.3: *Partitioning of mass-spring system (stable coupling).*

simultaneously with the solid body (the left-hand side of equation (3.12) and the left-hand rectangle in figure 3.3). The difference between the "frozen" liquid behaviour and the real liquid dynamics, oscillations around the frozen state, appears on the right-hand side of equation (3.12) and in the right-hand rectangle in figure 3.3. This quasi-simultaneous method makes the coupling stable and corresponds to system (3.8); here, also, the solid-body mass and the liquid mass are treated simultaneously as is reflected on the left-hand side of (3.8). In this system the "frozen" state is the position of the liquid with respect to the inertial reference frame; oscillations around this state correspond to the liquid dynamics with respect to the moving reference frame (as described by the velocity $\boldsymbol{u}$).

Stability Analysis

Apart from an intuitive approach, the stability of the two partitioning methods in this section can also be analysed mathematically. Hereto, equations (3.10a) and (3.12) are unified in a single equation

$$(m_s + \gamma m_l)\,\ddot{x}_s^{(n+1)} = -F^{(n)} + \gamma m_l \ddot{x}^{(n)},$$

where γ is a parameter indicating the type of partitioning; $\gamma = 0$ corresponds to a possibly unstable partitioning and $\gamma = 1$ to the stable partitioning. This equation is combined with (3.10b) and (3.10c) as before, which gives

$$\frac{m_l}{k}\ddot{F}^{(n+1)} + F^{(n+1)} = -(1-\gamma)\,\beta F^{(n)} + \gamma\beta\frac{m_l}{k}\ddot{F}^{(n)},$$

where a parameter $\beta = \beta(\gamma) = m_l/(m_s + \gamma m_l)$ has been introduced. After substitution of a discretised version of the second-order derivative with time step δt, *e.g.*

$$\ddot{F}^{(n)} = \frac{F^{(n)} - 2F^{(n-1)} + F^{(n-2)}}{\delta t^2},$$

and rearranging terms this results in

$$(\alpha+1)\,F^{(n+1)} + (\alpha\beta\,(1-\gamma) - \beta\gamma - 2)\,F^{(n)} + (2\beta\gamma+1)\,F^{(n-1)} - \beta\gamma F^{(n-2)} = 0,$$

where $\alpha = k\,\delta t^2/m_l$. The roots λ of this third-order difference equation satisfy

$$\alpha\lambda^3 + \alpha\beta\,(1-\gamma)\,\lambda^2 + (\lambda - \beta\gamma)\,(\lambda-1)^2 = 0.$$

For $\alpha = 0$ the roots are equal to $\lambda_{1,2} = 1$ and $\lambda_3 = \beta\gamma$. The latter root is always less than one since either $\gamma = 0$, whence $\lambda_3 = 0$, or $\gamma = 1$, whence $\lambda_3 = \beta = m_l/(m_s + m_l) < 1$. Hence, both the partitioning methods are stable for $\alpha = 0$. In the case $\alpha \to \infty$, two of the roots vanish, the other root equals $\lambda_3 = -\beta\,(1-\gamma)$. This root vanishes as well if $\gamma = 1$, making the second partitioning method stable for $\alpha \to \infty$. However, if $\gamma = 0$, then $\lambda_3 = -\beta = -m_l/m_s$. Thus, the first partitioning method, for $\alpha \to \infty$, is unstable if $m_l > m_s$; a result that has been noticed before.

3.3.3 Discretised Equations

Based on the stability of the different partitionings of the mass-spring model in the previous section, system (3.8) (rather than (3.5)) is the preferred model for the solid-body dynamics. Indeed, after discretisation, system (3.5) (where the left-hand side is evaluated at the new time level and the right-hand side at the old time level) corresponds to equations (3.10a) and (3.10b) in the sense that the solid-body mass appears on the left and the liquid mass on the right of the equality. On the other hand, in system (3.8), the total mass of the coupled system appears on the left-hand side, which corresponds to equation (3.12). In section 3.4.1 more details on the stability of systems (3.5) and (3.8) can be found.

In this section the discretisation of system (3.8) is discussed in more detail. The temporal discretisation of the equations for linear momentum (3.8a) and angular momentum (3.8b) is straightforward. Both the linear acceleration $d\boldsymbol{q}/dt$ and the angular acceleration $d\boldsymbol{\omega}/dt$ are discretised at the new time level (indicated by a superscript $n+1$). The linear and angular velocity are discretised at the old time level (indicated by a superscript n). Since the model for the solid-body dynamics is applied after the model for the liquid dynamics has been completed (in the same time step), all the quantities from the liquid model carry a superscript $n+1$. This results in

$$m\frac{d\boldsymbol{q}}{dt}^{n+1} + \frac{d\boldsymbol{\omega}}{dt}^{n+1} \times m\overline{\boldsymbol{r}}^{n+1} = \boldsymbol{\mathcal{L}}^n, \tag{3.14a}$$

$$m\overline{\boldsymbol{r}}^{n+1} \times \frac{d\boldsymbol{q}}{dt}^{n+1} + \boldsymbol{I}^{n+1}\frac{d\boldsymbol{\omega}}{dt}^{n+1} = \boldsymbol{\mathcal{A}}^n, \tag{3.14b}$$

where

$$\boldsymbol{\mathcal{L}}^n = -m\boldsymbol{\omega}^n \times \boldsymbol{q}^n - \boldsymbol{\omega}^n \times \left(\boldsymbol{\omega}^n \times m\overline{\boldsymbol{r}}^{n+1}\right) - \int_V \rho\boldsymbol{\mathcal{U}}^{n+1}\,dV + m_s\boldsymbol{F}^{n+1}, \tag{3.15a}$$

$$\boldsymbol{\mathcal{A}}^n = -m\overline{\boldsymbol{r}}^{n+1} \times (\boldsymbol{\omega}^n \times \boldsymbol{q}^n) - \boldsymbol{\omega}^n \times \boldsymbol{I}^{n+1}\boldsymbol{\omega}^n - \int_V \rho\boldsymbol{r}^{n+1} \times \boldsymbol{\mathcal{U}}^{n+1}\,dV + m_s\overline{\boldsymbol{r}}_s \times \boldsymbol{F}^{n+1}. \tag{3.15b}$$

In these equations $\boldsymbol{\mathcal{U}}^{n+1} = D\boldsymbol{u}^{n+1}/Dt + 2\boldsymbol{\omega}^n \times \boldsymbol{u}^{n+1} - \boldsymbol{F}^{n+1}$. Note that the volume V is the volume of the solid body (recall that the volume integral was deduced, via the divergence theorem, from a boundary integral over the boundary of the solid body). Hence, this volume V does not carry a superscript since it does not depend on time. However, in that part of the solid body where liquid is absent, the integrand vanishes because the density is taken to be equal to zero in the void region.

The implementation of the non-integral terms in (3.14) and (3.15) is trivial. The implementation of the remaining terms, although being far from difficult, requires some attention. All these terms are of the form $\int_V \rho\varphi^n \, dV$ and are discretised as

$$\int_V \rho\varphi^n \, dV \doteq \sum_{i,j,k} \rho\varphi^n_{i,j,k} F^s_{i,j,k} \delta x_i \delta y_j \delta z_k, \tag{3.16}$$

where the summation is over all the computational cells, φ is some scalar variable (*e.g.* Du/Dt), $F^s_{i,j,k}$ is the volume-of-fluid function in cell (i,j,k), and $\delta x_i \delta y_j \delta z_k$ is the volume of this cell. The variable φ is evaluated in cell centres. This means that staggered velocities have to be averaged before they can be evaluated. Note that also the centre of mass $\overline{\boldsymbol{r}}_l$ and the moment-of-inertia tensor $\boldsymbol{I}_l$ of the liquid are integral terms since

$$m_l \overline{\boldsymbol{r}}_l = \int_V \rho \boldsymbol{r} \, dV \quad \text{and} \quad \boldsymbol{I}_l \boldsymbol{\psi} = \int_V \rho \boldsymbol{r} \times (\boldsymbol{\psi} \times \boldsymbol{r}) \, dV,$$

where $\boldsymbol{\psi}$ is some vector (*e.g.* $d\boldsymbol{\omega}/dt$) the moment-of-inertia tensor operates on. Therefore, these quantities are computed using (3.16) as well.

3.3.4 Solution Method

In matrix form the 6×6 linear system (3.14) for the unknown vectors $(d\boldsymbol{q}/dt)^{n+1}$ and $(d\boldsymbol{\omega}/dt)^{n+1}$ reads

$$\begin{pmatrix} m & 0 & 0 & 0 & m\overline{r}_z & -m\overline{r}_y \\ 0 & m & 0 & -m\overline{r}_z & 0 & m\overline{r}_x \\ 0 & 0 & m & m\overline{r}_y & -m\overline{r}_x & 0 \\ 0 & -m\overline{r}_z & m\overline{r}_y & I_{xx} & -I_{xy} & -I_{xz} \\ m\overline{r}_z & 0 & -m\overline{r}_x & -I_{xy} & I_{yy} & -I_{yz} \\ -m\overline{r}_y & m\overline{r}_x & 0 & -I_{xz} & -I_{yz} & I_{zz} \end{pmatrix} \begin{pmatrix} dq_x/dt \\ dq_y/dt \\ dq_z/dt \\ d\omega_x/dt \\ d\omega_y/dt \\ d\omega_z/dt \end{pmatrix} = \begin{pmatrix} \mathcal{L}_x \\ \mathcal{L}_y \\ \mathcal{L}_z \\ \mathcal{A}_x \\ \mathcal{A}_y \\ \mathcal{A}_z \end{pmatrix}. \tag{3.17}$$

For presentational reasons the superscripts have been dropped (it will be clear that the matrix and right-hand side are evaluated at time level n, while the unknown vector contains quantities at time level $n+1$). Further, the components of a vector $\boldsymbol{\psi}$ are denoted with subscripts x, y, and z, *i.e.* $\boldsymbol{\psi} = (\psi_x, \psi_y, \psi_z)^T$, and the moment-of-inertia tensor has components

$$\boldsymbol{I} = \begin{pmatrix} I_{xx} & -I_{xy} & -I_{xz} \\ -I_{xy} & I_{yy} & -I_{yz} \\ -I_{xz} & -I_{yz} & I_{zz} \end{pmatrix}.$$

By using Gaussian elimination, the lower-left 3×3 block of the matrix in (3.17) is eliminated, whence a decoupled system for $d\boldsymbol{\omega}/dt$ arises, namely

$$\left(\begin{array}{ccc|c} I_{xx} - m\overline{r}_y^2 - m\overline{r}_z^2 & -I_{xy} + m\overline{r}_x\overline{r}_y & -I_{xz} + m\overline{r}_x\overline{r}_z & \mathcal{A}_x + \overline{r}_z\mathcal{L}_y - \overline{r}_y\mathcal{L}_z \\ -I_{xy} + m\overline{r}_x\overline{r}_y & I_{yy} - m\overline{r}_x^2 - m\overline{r}_z^2 & -I_{yz} + m\overline{r}_y\overline{r}_z & \mathcal{A}_y - \overline{r}_z\mathcal{L}_x + \overline{r}_x\mathcal{L}_z \\ -I_{xz} + m\overline{r}_x\overline{r}_z & -I_{yz} + m\overline{r}_y\overline{r}_z & I_{zz} - m\overline{r}_x^2 - m\overline{r}_y^2 & \mathcal{A}_z + \overline{r}_y\mathcal{L}_x - \overline{r}_x\mathcal{L}_y \end{array}\right). \quad (3.18)$$

Note that during this process no divisions (in particular through zero) take place. Using Steiner's theorem, it follows that the 3×3 matrix in (3.18) is the moment-of-inertia tensor relative to the centre of mass of the coupled system. The 3×3 linear system for $d\boldsymbol{\omega}/dt$ is solved with Gaussian elimination followed by backward substitution. Once the solution for $d\boldsymbol{\omega}/dt$ is known, the solution for $d\boldsymbol{q}/dt$ can be found using backward substitution in (3.17).

In the model for the solid-body dynamics and also in the Navier-Stokes equations (3.3) the linear and angular velocity of the solid body appears. This means that $d\boldsymbol{q}^{n+1}/dt$ and $d\boldsymbol{\omega}^{n+1}/dt$ have to be integrated in time, which is done using a fourth-order Runge-Kutta method. Hereto, system (3.17) is written as

$$\frac{d\boldsymbol{y}}{dt} = \boldsymbol{g}\left(t, \boldsymbol{y}\right), \quad (3.19)$$

where $\boldsymbol{y} = (\boldsymbol{q}, \boldsymbol{\omega})^T$ and $\boldsymbol{g} = \boldsymbol{M}^{-1}\left(\boldsymbol{\mathcal{L}}, \boldsymbol{\mathcal{A}}\right)^T$. The matrix $\boldsymbol{M}$ is an abbreviation for the matrix that appears in (3.17). Equation (3.19) is integrated in time from level n to level $n+1$ by

$$\boldsymbol{y}^{n+1} = \boldsymbol{y}^n + \frac{1}{6}\delta t\left(\boldsymbol{S}_1 + 2\boldsymbol{S}_2 + 2\boldsymbol{S}_3 + \boldsymbol{S}_4\right),$$

where the four stages $\boldsymbol{S}_1, \ldots, \boldsymbol{S}_4$ are defined as

$$\begin{aligned} \boldsymbol{S}_1 &= \boldsymbol{g}\left(t^n, \boldsymbol{y}^n\right), \\ \boldsymbol{S}_2 &= \boldsymbol{g}\left(t^n + \frac{1}{2}\delta t, \boldsymbol{y}^n + \frac{1}{2}\delta t\boldsymbol{S}_1\right), \\ \boldsymbol{S}_3 &= \boldsymbol{g}\left(t^n + \frac{1}{2}\delta t, \boldsymbol{y}^n + \frac{1}{2}\delta t\boldsymbol{S}_2\right), \\ \boldsymbol{S}_4 &= \boldsymbol{g}\left(t^n + \delta t, \boldsymbol{y}^n + \delta t\boldsymbol{S}_3\right). \end{aligned}$$

Note that the explicit time dependence in the right-hand side of (3.19) (*i.e.* the first component of the function $\boldsymbol{g}$) is entirely due to the liquid model. Since the models for the liquid dynamics and the solid-body dynamics are treated separately, it is most unconvenient to evaluate the position and velocity of the liquid at the intermediate time level $n + \frac{1}{2}$. Moreover, the quantities of the liquid model are already known at time level $n+1$. Hence, in the Runge-Kutta stages $\boldsymbol{S}_1, \ldots, \boldsymbol{S}_4$, the first component of $\boldsymbol{g}$ is frozen at time level $n+1$.

In the simulations that have been performed with the method presented in this chapter, the solid-body dynamics turns out to be more sensitive to small disturbances than the model for the liquid dynamics, hence requiring either a smaller time step or a more accurate time-integration method. Since the latter option has been implemented, in practice, it is possible to set the time step for the solid-body model equal to the one used

in the liquid model. Should this not be sufficient, then it is possible to take multiple Runge-Kutta time steps during one single time step in the liquid model.

Now that $d\boldsymbol{q}/dt$, $d\boldsymbol{\omega}/dt$, $\boldsymbol{q}$, and $\boldsymbol{\omega}$ are known at the new time level, one computational cycle has been finished.

3.4 Results

3.4.1 Free Fall

Stable Method

As a first example, the free fall of a rectangular tank, partially filled with liquid, is simulated. With this simulation some basic validation is performed. Consider a hollow, rectangular tank with dimensions $1 \times 2 \times 4$. The mass of the tank is set to $m_s = 12$. From these parameters the moment-of-inertia tensor of the tank, relative to the centre of mass of the tank, can be computed, namely $\boldsymbol{I}_s = \mathrm{diag}\,(36, 25, 9)$. The lower half (in z-direction) of the tank is filled with liquid having a density of $\rho = 6$. Hence, the liquid mass is equal to $m_l = 24$ and the total mass equals $m = 36$. The acceleration $\boldsymbol{F}$ due to gravity is set to $(0, 0, -10)^T$.

During the first 0.05 seconds of the simulation (on a computational grid of $10 \times 20 \times 40$ cells) the tank is kept at its initial position, whence the pressure settles itself at hydrostatic values. After 0.05 seconds, the tank, together with the liquid, is released. This, of course, causes the coupled system to fall in the negative z-direction with an acceleration equal to gravitational acceleration. Also, the pressure becomes equal to the ambient pressure $p_0 = 0$ everywhere in the fluid since the coupled system is in a free fall. These results are confirmed in figure 3.4. On the left in this figure, the pressure is plotted at equidistant locations along the centreline in z-direction. At the bottom of the tank the pressure is equal to $p = 6 \cdot 10 \cdot 2 = 120$. Taking into account that the centre of the first computational

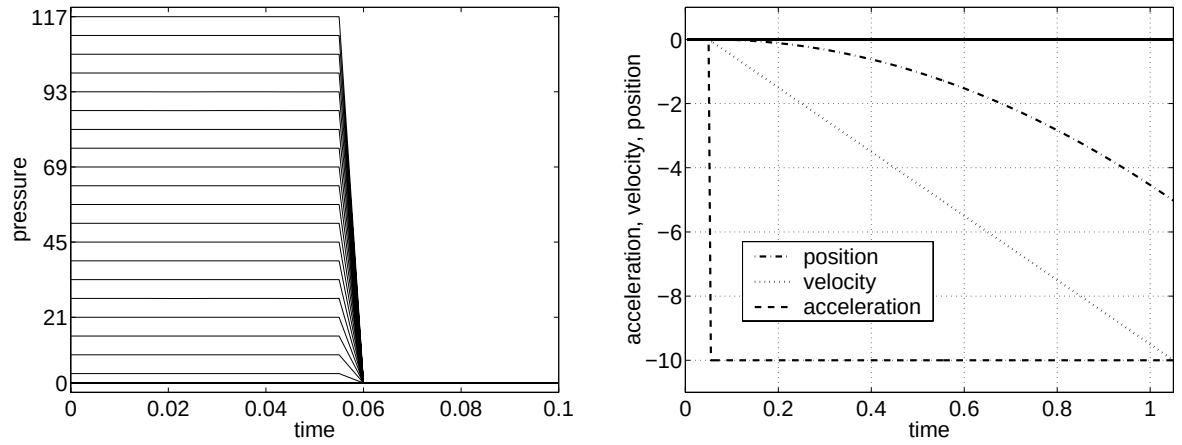

Figure 3.4: *Left: Pressure at equidistant locations along the z-centreline of the tank as a function of time. Right: Acceleration (dashed), velocity (dotted), and position (dash-dotted) in z-direction of the coupled system as a function of time. The solid line represents the same quantities in x- and y-direction.*

cell lies half a mesh size (which is $\delta z/2 = 0.05$) above the bottom of the tank, the maximum value of $p = 117$ in figure 3.4 can be explained. The same reasoning applies to the centre of the last cell below the free surface, where the pressure is equal to $p = 3$ (at the free surface the pressure has a value of $p = p_0 = 0$). Since the tank is kept at its initial position until $t = 0.05$, the pressure in the tank does not change in this interval. Also, one time step after $t = 0.05$ (the time step is set to $\delta t = 0.005$), the pressure has not changed since, in the liquid model, the virtual body force (3.4) is discretised at the old time level at which time the tank was not moving. In the next time step, at $t = 0.06$, the fluid "feels" that the tank is falling with an acceleration of $d\boldsymbol{q}/dt = (0, 0, -10)^T$, whence the pressure in the fluid becomes zero everywhere. On the right in figure 3.4 the motion of the tank is plotted. Most of the quantities, namely the angular acceleration, velocity, and position in all three spatial directions and the linear acceleration, velocity, and position in x- and y-direction are equal to zero during the entire simulation. The linear acceleration in z-direction changes from 0 to -10 at $t = 0.05$ as expected. Also the linear velocity and position in z-direction, showing linear and quadratic behaviour, are plotted. Note that, for presentational reasons, the initial position of the tank is set to zero in this figure.

Of course, the results from this simulation should be independent of the choice for the moving reference frame. To check this, the previous simulation is performed for two different cases. In the first case, the origin of the moving reference frame is equal to the centre of mass of the coupled system. In the second case, the origin is chosen such that the centre of mass of the tank is located at $\overline{\boldsymbol{r}}_s = (1, 2, 4)^T$. In the first case, system (3.17) is diagonal since $\overline{\boldsymbol{r}} = (0, 0, 0)^T$ and the moment-of-inertia tensor of the coupled system is diagonal (the coordinate system is aligned with the principal axes of the coupled system). Hence, in this case, system (3.18) is equal to the lower-right block of (3.17). In the second case, $\overline{\boldsymbol{r}} = (1, 2, 4/3)^T$ and $\boldsymbol{I}$ is not diagonal. Hence, system (3.17) is not diagonal and Gaussian elimination is needed to achieve a diagonal system (3.18) (again, the coordinate system is aligned with the principal axes). The 3×3 systems for $d\boldsymbol{\omega}/dt$ for these cases, taken from the simulation and rounded to two decimal places, are

$$\left(\begin{array}{ccc|c} 59.96 & 2.76E-08 & 9.59E-07 & -2.74E-04 \\ 2.76E-08 & 42.96 & -7.88E-07 & 4.10E-06 \\ 9.59E-07 & -7.88E-07 & 18.96 & -5.64E-05 \end{array}\right)$$

and

$$\left(\begin{array}{ccc|c} 59.96 & 9.77E-04 & 7.63E-04 & 2.62E-03 \\ 9.77E-04 & 42.96 & 1.89E-03 & -7.63E-04 \\ 7.63E-04 & 1.89E-03 & 18.96 & -5.64E-05 \end{array}\right).$$

respectively. Analytically, in both cases, system (3.18) equals

$$\left(\begin{array}{ccc|c} 60 & 0 & 0 & 0 \\ 0 & 43 & 0 & 0 \\ 0 & 0 & 19 & 0 \end{array}\right).$$

The numerical results agree closely with theory; minor differences are due to the numerical integration method (3.16) for computing the centre of mass and the moment-of-inertia tensor of the liquid. This simulation has been repeated for liquid/solid mass ratios ranging

from 0.1 to 100. For all mass ratios the method gave stable results identical to figure 3.4 (only the value of the pressure in the fluid differed because of the change in the density of the fluid).

Unstable Method

The previous simulation has been performed with the possibly unstable method (3.5) as well. For this method the acceleration of the coupled system with a liquid/solid mass ratio of 1.2 is shown in figure 3.5. If the liquid/solid mass ratio is further decreased to

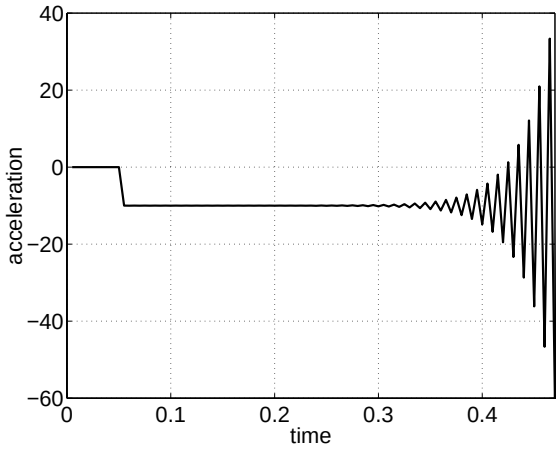

Figure 3.5: *Acceleration in z-direction of the coupled system as a function of time as predicted by the unstable method.*

one, then the unstable method gives the same results as the stable method. This can be explained by analysing equations (3.5a) and (3.8a). In the absence of angular motion these equations reduce to

$$m_s \frac{d\boldsymbol{q}}{dt} = -\int_V \rho \left(\frac{D\boldsymbol{v}}{Dt} - \boldsymbol{F} \right) dV + m_s \boldsymbol{F}$$

and

$$m \frac{d\boldsymbol{q}}{dt} = -\int_V \rho \left(\frac{D\boldsymbol{u}}{Dt} - \boldsymbol{F} \right) dV + m_s \boldsymbol{F},$$

respectively, where, using equation (3.1), the relation between $\boldsymbol{u}$ and $\boldsymbol{v}$ is given by $D\boldsymbol{v}/Dt = d\boldsymbol{q}/dt + D\boldsymbol{u}/Dt$. These equations are discretised by evaluating the left-hand side at the new time level $n+1$ and the right-hand side at the old time level n, *i.e.*

$$m_s \frac{d\boldsymbol{q}}{dt}^{n+1} = -\int_V \rho \left(\frac{D\boldsymbol{v}^n}{Dt} - \boldsymbol{F} \right) dV + m_s \boldsymbol{F}$$

and

$$m \frac{d\boldsymbol{q}}{dt}^{n+1} = -\int_V \rho \left(\frac{D\boldsymbol{u}^n}{Dt} - \boldsymbol{F} \right) dV + m_s \boldsymbol{F}.$$

If both the liquid velocity $\boldsymbol{u}$ with respect to the moving reference frame and the pressure p vanish throughout the liquid (as is the case in this section), then these equations simplify to

$$m_s \frac{d\boldsymbol{q}}{dt}^{n+1} = -m_l \frac{d\boldsymbol{q}}{dt}^{n} + m_l \boldsymbol{F} + m_s \boldsymbol{F} \quad \text{and} \quad m \frac{d\boldsymbol{q}}{dt}^{n+1} = m_l \boldsymbol{F} + m_s \boldsymbol{F},$$

which is rewritten as

$$\frac{d\boldsymbol{q}}{dt}^{n+1} = -\frac{m_l}{m_s}\left(\frac{d\boldsymbol{q}}{dt}^{n} - \boldsymbol{F}\right) + \boldsymbol{F} \quad \text{and} \quad \frac{d\boldsymbol{q}}{dt}^{n+1} = \boldsymbol{F}.$$

Clearly, the solution for both formulations is $d\boldsymbol{q}/dt \equiv \boldsymbol{F}$. However, small disturbances in the solution for $d\boldsymbol{q}/dt$ at time level n are in the first formulation amplified with a factor m_l/m_s (this factor is visible in figure 3.5, where $m_l/m_s = 1.2$), which becomes unstable if the liquid/solid mass ratio exceeds unity in correspondence with the numerical results (see also the analysis of the mass-spring model in section 3.3.2).

3.4.2 Empty Tank

Another method for validating the model for the solid-body dynamics is by studying the motion of a (rectangular) tank that is not filled with liquid. If the moving origin coincides with the centre of mass of the tank, *i.e.* $\overline{\boldsymbol{r}}_s = (0,0,0)^T$, and the acceleration $\boldsymbol{F}$ is set to zero, then system (3.8) simplifies to

$$m_s \frac{d\boldsymbol{q}}{dt} = -m\boldsymbol{\omega} \times \boldsymbol{q},$$
$$\boldsymbol{I}_s \frac{d\boldsymbol{\omega}}{dt} = -\boldsymbol{\omega} \times \boldsymbol{I}_s \boldsymbol{\omega}.$$

Note that, because of the absence of liquid, m and $\boldsymbol{I}$ have been replaced by m_s and $\boldsymbol{I}_s$ respectively. The initial conditions are chosen as $\boldsymbol{q}(0) = (0,0,0)^T$ and $\boldsymbol{\omega}(0) = \left(\omega_x^0, \omega_y^0, \omega_z^0\right)^T$. The former initial condition implies that $\boldsymbol{q}$ is identically equal to zero. Since the moving origin was chosen to coincide with the centre of mass of the tank, the moment-of-inertia tensor of the tank is diagonal, say $\boldsymbol{I}_s = \mathrm{diag}(I_{xx}, I_{yy}, I_{zz})$. Hence, the following three equations remain

$$\frac{d\omega_x}{dt} = \frac{I_{yy} - I_{zz}}{I_{xx}}\omega_y\omega_z, \quad \frac{d\omega_y}{dt} = \frac{I_{zz} - I_{xx}}{I_{yy}}\omega_x\omega_z, \quad \frac{d\omega_z}{dt} = \frac{I_{xx} - I_{yy}}{I_{zz}}\omega_x\omega_y. \tag{3.21}$$

Harmonic Solutions

Obviously, the tank keeps rotating with the initial angular velocity if two components of $\boldsymbol{\omega}(0)$ are set to zero. Hence, the initial angular velocity is set to $\boldsymbol{\omega}(0) = (2,0,1)^T$. Further, the moment-of-inertia tensor (relative to the centre of mass) is set to $\boldsymbol{I}_s = \mathrm{diag}(1, 1, \pi/2 + 1)$ (note that also in the case $I_{xx} = I_{yy} = I_{zz}$ the tank keeps rotating with the initial angular velocity). With these conditions the solution of (3.21) can be found analytically, namely

$$\omega_x(t) = 2\cos\left(\frac{\pi}{2}t\right), \quad \omega_y(t) = 2\sin\left(\frac{\pi}{2}t\right), \quad \omega_z(t) = 1.$$

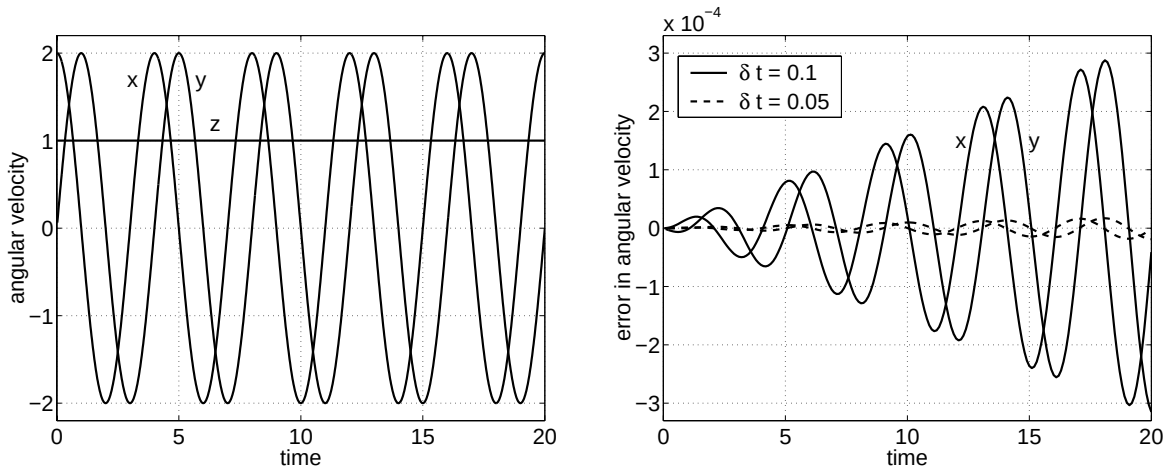

Figure 3.6: *Left: Evolution of the angular velocity around the three Cartesian axes for an empty tank with* $\boldsymbol{I}_s = \mathrm{diag}\,(1, 1, \pi/2 + 1)$ *and* $\boldsymbol{\omega}\,(0) = (2, 0, 1)^T$. *Right: Evolution of the error in the angular velocity around the x- and y-axis for two different time steps,* $\delta t = 0.1$ *(large error) and* $\delta t = 0.05$ *(small error).*

Results of the numerical simulation are shown in figure 3.6. On the left, lines indicated with x, y, and z show the numerical solutions for ω_x, ω_y, and ω_z respectively. On the right, the error in the solutions for ω_x and ω_y is plotted for two different time steps, $\delta t = 0.1$ and $\delta t = 0.05$. Due to the fourth-order Runge-Kutta time integration, the error in the simulation corresponding to $\delta t = 0.1$ is 16 times larger than the one corresponding to $\delta t = 0.05$.

Nonharmonic Solutions

If I_{xx}, I_{yy}, and I_{zz} are pairwise unequal, then (3.21) is more difficult to solve. Hence, only the conservation of kinetic energy is checked in this case, which is given by

$$E_{\mathrm{kin}} = \frac{1}{2} I_{xx} \omega_x^2 + \frac{1}{2} I_{yy} \omega_y^2 + \frac{1}{2} I_{zz} \omega_z^2.$$

On the left in figure 3.7 the numerical solutions for ω_x, ω_y, and ω_z are shown in the case that $\boldsymbol{I}_s = \mathrm{diag}\,(1, 2, 4)$ and $\boldsymbol{\omega}\,(0) = (3, 2, 1)^T$. In this figure the kinetic energy minus the initial kinetic energy is plotted as a dashed line, which is clearly equal to zero during the entire simulation. A nice way to visualise the angular velocity is shown on the right in figure 3.7, where the projection $\boldsymbol{\omega}/|\boldsymbol{\omega}|$ of the angular velocity on the unit sphere is plotted. In the bounding box of this figure the projections of the normalised angular velocity in the xy-, xz-, and yz-plane are plotted.

3.4.3 Full Tank

In this section the motion of the same container as in the previous section is studied, *i.e.* with mass $m_s = 12$ and moment-of-inertia tensor $\boldsymbol{I}_s = \mathrm{diag}\,(1, 2, 4)$. However, now the container is completely filled with liquid. A simple calculation shows that the moment-of-inertia tensor of the liquid in this case is equal to $\boldsymbol{I}_l = \frac{1}{12} m_l \,\mathrm{diag}\left(\frac{7}{2} - 2\sqrt{2}, \frac{3}{2}, \frac{7}{2} - \sqrt{2}\right)$.

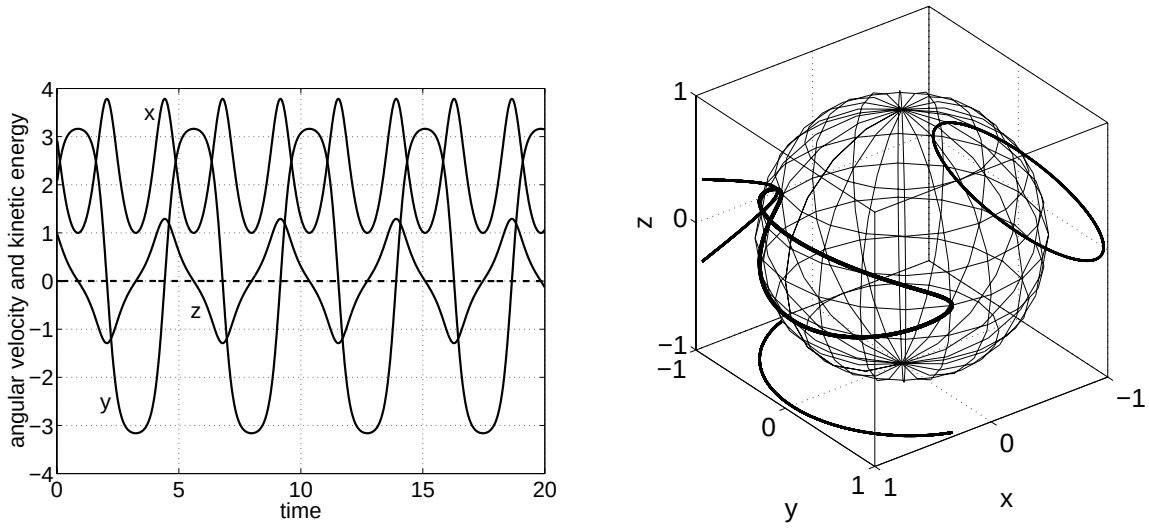

Figure 3.7: *Left: Evolution of the angular velocity (solid lines) around the three Cartesian axes for an empty tank with* $\boldsymbol{I}_s = \mathrm{diag}\,(1,2,4)$ *and* $\boldsymbol{\omega}\,(0) = (3,2,1)^T$*. The dashed line represents the kinetic energy minus the initial kinetic energy of the container. Right: Projection of the angular velocity on the unit sphere.*

The presence of fluid leads to a totally different motion of the container compared to the results in the previous section. Indeed, the coupled system settles itself in a state of minimum kinetic energy, which corresponds to rotation around the axis with maximum moment of inertia (the fluid is responsible for damping the rotation around the x- and y-axis). Thus, in the steady-state solution, the system rotates around the z-axis only. The final angular velocity around this axis follows from conservation of angular momentum. If the initial angular velocity is, again, chosen as $\boldsymbol{\omega}\,(0) = (3,2,1)^T$ and the liquid mass is set to $m_l = 120$ (*i.e.* a liquid/solid mass ratio of 10), then, theoretically, the final angular velocity around the z-axis is equal to 1.93. The results for this particular simulation are shown in figure 3.8. On the left, the angular velocities around the x-, y-, and z-axis are plotted versus time as well as the theoretically predicted final angular velocity around the z-axis. On the right, the projection of the angular velocity on the unit sphere is plotted. From these figures the transition to rotation around a single axis becomes very clear. The numerical simulation predicts a final angular velocity around the stable moment-of-inertia axis in close correspondence with the theoretical value; the difference is less than half a percent.

Grid-Refinement Study and Time-Step Analysis

Now that the container is filled with liquid, a grid-refinement study and a time-step analysis can be performed. The above simulation is repeated on grids consisting of $20 \times 20 \times 20$, $40 \times 40 \times 40$, $60 \times 60 \times 60$, and $80 \times 80 \times 80$ computational cells. The results are shown in figure 3.9 (for presentational reasons only the angular velocity around the x-axis on the four different grids is considered). On the right in this figure the solutions on subsequent grids are subtracted from each other, giving an indication of the error in the numerical solution. Clearly, the error decreases when the grid is refined. Note that

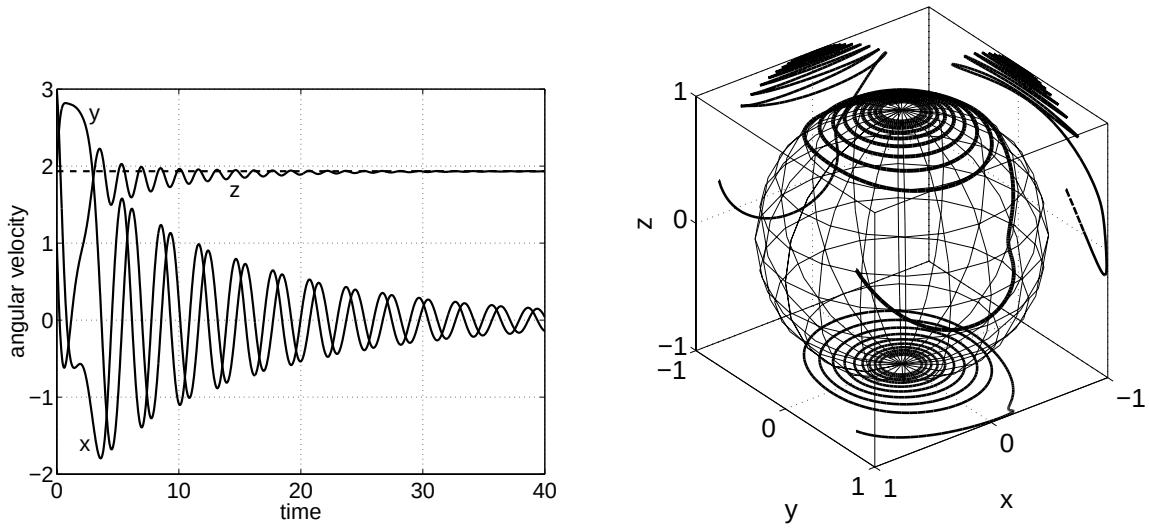

Figure 3.8: *Left: Evolution of the angular velocity (solid lines) around the three Cartesian axes for a completely filled tank. The dashed line represents the theoretically predicted final angular velocity around the z-axis. Right: Projection of the angular velocity on the unit sphere.*

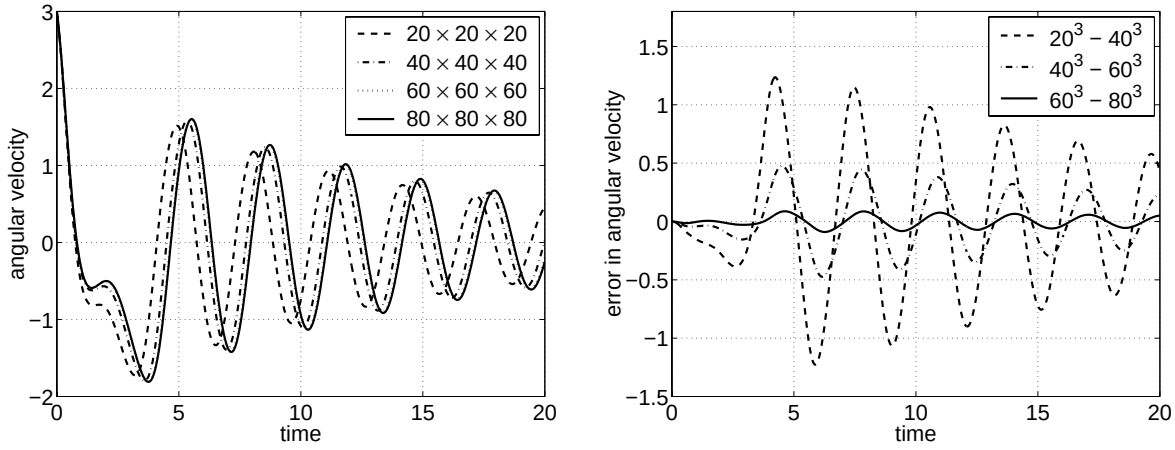

Figure 3.9: *Left: Angular velocity around x-axis of a full tank for various grids. Right: Indication of the error in the angular velocity given by the difference in the solutions on subsequent grids.*

the large size of the error can be explained by the phase difference between the solutions on the various grids.

All the simulations in this section have been performed with a time step of $\delta t = 10^{-3}$. In figure 3.10 the previous simulation is repeated on a grid of $40 \times 40 \times 40$ cells, but with different time steps, namely $\delta t = 5 \times 10^{-3}$, $\delta t = 1 \times 10^{-3}$, and $\delta t = 2 \times 10^{-4}$. The right-hand figure shows that the error in the angular velocity decreases when the time step is reduced.

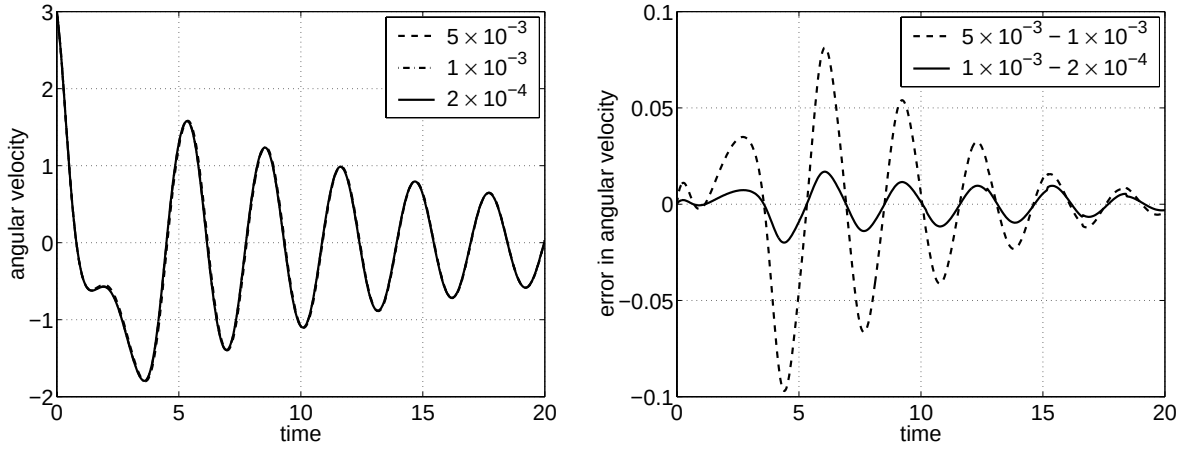

Figure 3.10: *Same as figure 3.9 but now for different time steps.*

Liquid/Solid Mass Ratio

Since the grid-refinement study and the time-step analysis revealed that the method is consistent, it is possible to examine how the coupled system that has been examined in this section reacts to a change in physical parameters, such as the liquid/solid mass ratio. In the previous simulations the liquid/solid mass ratio was equal to 10; the liquid mass and the solid-body mass were set to $m_l = 120$ and $m_s = 12$ respectively. If the liquid/solid mass ratio is increased (by increasing the density of the fluid), the fluid has more influence on the motion of the coupled system, whence the system settles itself faster into a steady state. On the other side, if the liquid/solid mass ratio is decreased, the system bears more resemblance to the motion of an empty tank. This phenomenon is illustrated on the left in figure 3.11, where the angular velocity of the coupled system is shown for liquid/solid mass ratios of 0.1, 1, 10, and 100. Note that the angular velocity converges to different values for different mass ratios, which is caused by a change in the liquid mass and thus the moment-of-inertia tensor. For presentational reasons only a detail of the time history of the angular velocity is shown in this figure. In the actual simulation the computation was continued until the amplitude of the oscillations in the angular velocity around the z-axis was less than 10^{-2} (for the simulation with a mass ratio of 0.1 this happened after approximately 400 seconds simulation time). On the right in figure 3.11 the computed angular velocity in the steady-state solution is compared to theory. Only the absolute value of the angular velocity is considered since the coupled system may be rotating in either positive or negative direction in the body-fixed coordinate system. The difference between simulation and theory is less than half a percent for all four mass ratios.

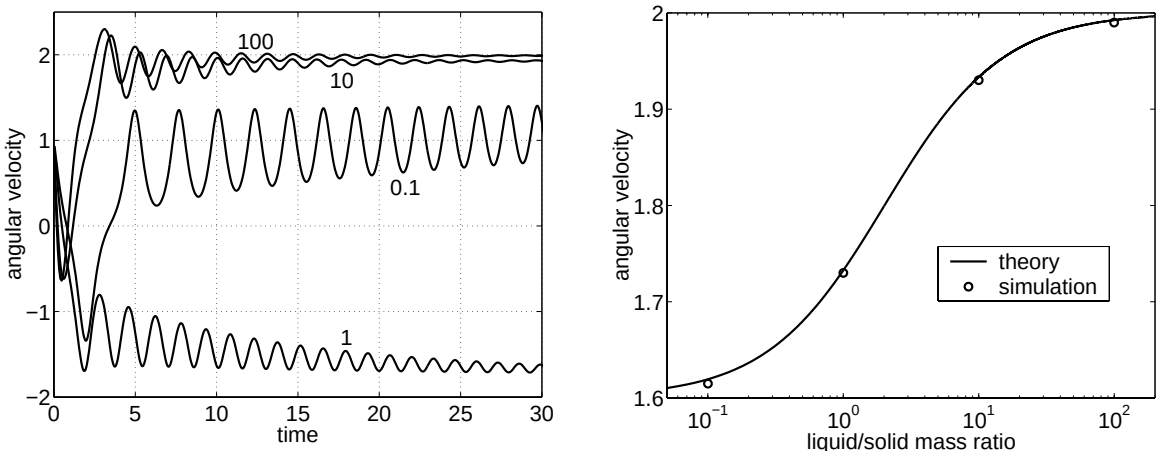

Figure 3.11: *Left: Evolution of the angular velocity around z-axis of a full tank for various liquid/solid mass ratios. Right: Comparison of the theoretical and numerical final angular velocity around z-axis.*

Although in this section only angular motion has been presented, in all the simulations the linear motion (which should be equal to zero) was computed from equation (3.8a). The linear acceleration turned out to be in the order of 10^{-6} for all the simulations in this section; the tolerance that was used in the computations. Thus, also the linear acceleration is predicted correctly in these simulations.

3.4.4 Partially Filled Tank

After studying an empty tank and a completely filled tank, in this section the intermediate case, a partially filled tank, is discussed. As an example a flat-spin motion is simulated. The same rectangular container that has been studied before is rotating around the x-axis with angular velocity $\omega_x = 5$ (initially, both ω_y and ω_z are equal to zero). The container is filled with fluid for $|y| \geq c$, where c determines the filling ratio. Since $I_{xx} < I_{yy} < I_{zz}$, rotation around the x-axis and z-axis is stable. However, because of the viscous liquid, kinetic energy is dissipated. Hence, in the steady state, the system will be rotating around the z-axis only, which corresponds to a state of minimum kinetic energy. This phenomenon — transition from rotation around the axis with minimum moment of inertia to rotation around the axis with maximum moment of inertia — is known as a flat spin. The concept of a flat spin is illustrated in figure 3.12. In the computation, the filling ratio was set to 65% and the density of the fluid was chosen such that the liquid/solid mass ratio equals $m_l/m_s = 10$. In figure 3.13 the angular velocities around the Cartesian axes are shown as a function of time. This figure clearly shows that some time (more than ten seconds) is needed before the transition is triggered. Once rotation around the y- and z-axis is excited, the change of rotation axis takes place in about ten seconds, although quite some time passes before the angular velocities around the x- and y-axis decrease to zero.

In figure 3.14 a more detailed study of the steady rotation around the x-axis at the beginning and around the z-axis at the end of the simulation is shown. In this figure snapshots of the free surface (solid lines) are drawn; on the left the results from the

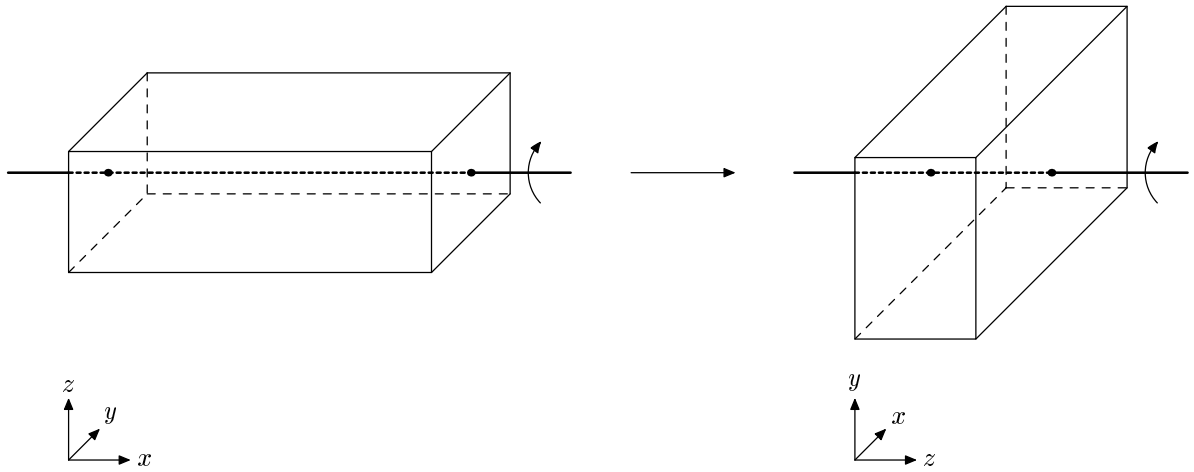

Figure 3.12: *Flat spin; change of rotation around axis with minimum moment of inertia to rotation around axis with maximum moment of inertia.*

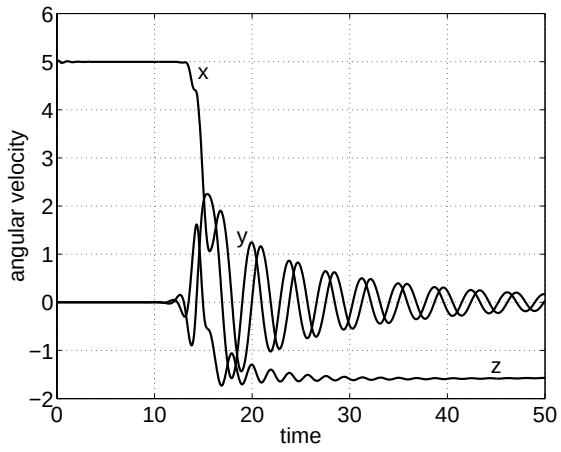

Figure 3.13: *Evolution of the angular velocity around the three Cartesian axes for a partially filled tank.*

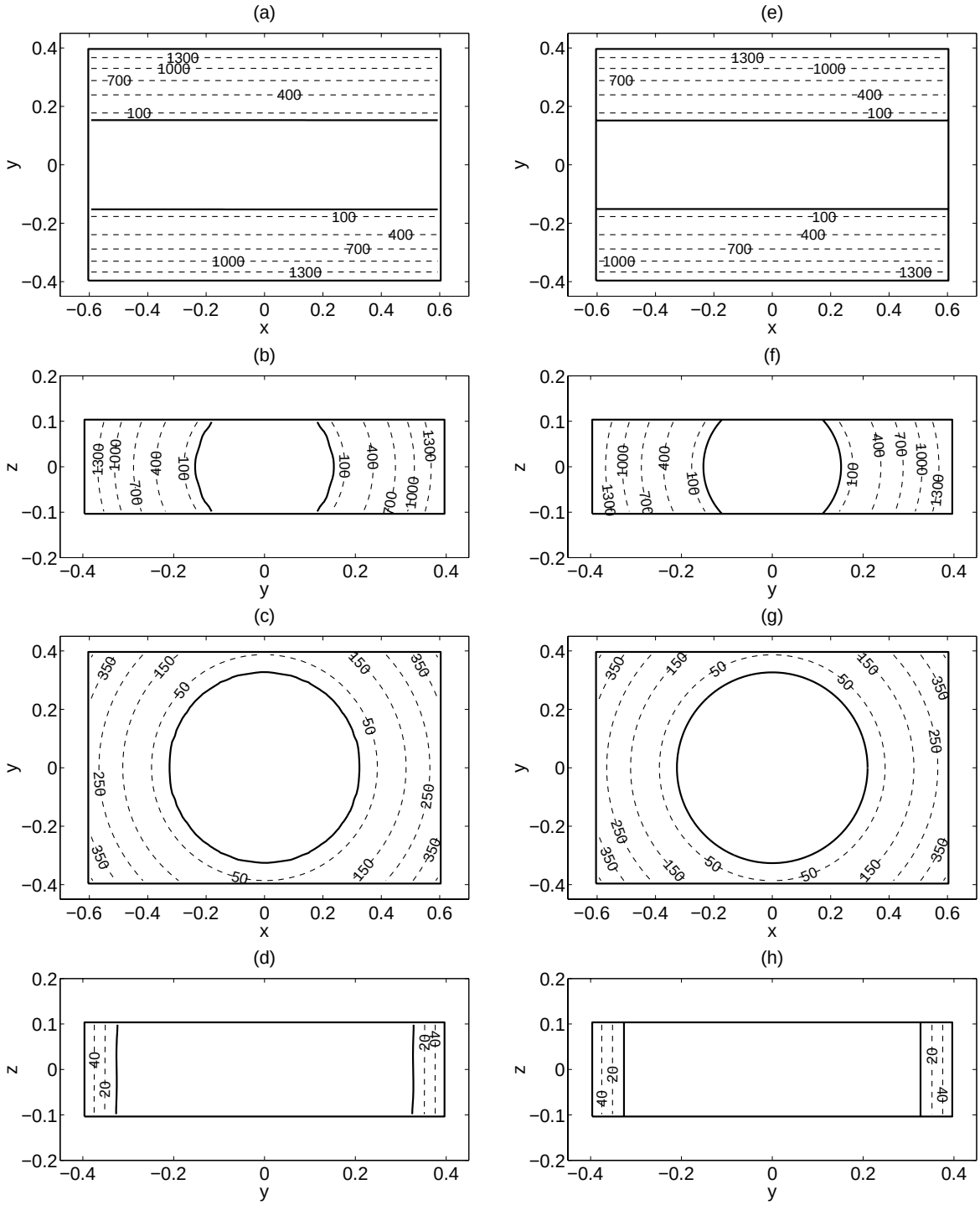

Figure 3.14: *Snapshots of the free surface (solid lines) and pressure contours (dashed lines) for the flat-spin motion in the xy- and yz-plane at two different time levels, namely at the beginning (top four) and at the end (bottom four) of the flat spin. On the left results from the simulation, on the right results based on theory.*

simulation and on the right the corresponding plots based on theory are shown. The results in two different cross sections, namely in the xy- and the yz-plane, and at two different time levels, namely at the beginning and at the end of the simulation, are presented. This figure clearly shows that initially the system is rotating around the x-axis and finally around the z-axis. Indeed, in the xy-plane the shape of the free surface changes from a straight line into a circle, while in the yz-plane opposite behaviour takes place.

When the system is rotating around one axis only, *i.e.* at the beginning and at the end of the simulation, it is easy to compare the pressure contours to theory since in this case the pressure contours are concentric circles around the axis of rotation. If the pressure at the free surface is equal to zero, then the pressure p at distance R from the centre of rotation is equal to

$$p = \frac{1}{2}\rho\,\omega^2\left(R^2 - r^2\right),$$

where ρ is the density of the fluid, ω is the angular velocity, and r is the distance between the free surface and the centre of rotation. This theory is compared to results from the numerical simulation in figure 3.14 as well, where the pressure contours are plotted as dashed lines. Obviously, the correspondence between simulation and theory is very good.

In figure 3.15 three-dimensional snapshots of a flat-spin simulation are shown, for which the filling ratio was decreased to 40%. In the upper-left snapshot, the container is rotating steadily around the axis with minimum moment of inertia. In the second snapshot, the beginning of the flat spin can be seen; liquid starts to flow due to rotation around the y- and z-axis. Some intermediate snapshots show the violent behaviour of the transition. Finally, in the lower-right snapshot, the angular velocities around the x- and y-axis have vanished and the container is rotating steadily around the axis with maximum moment of inertia.

3.4.5 The Wet Satellite Model Experiment

For studying the dynamics of liquid-filled spacecraft, the Wet Satellite Model (WSM) experiment was performed in 1992 [86]. Following the launch of the MASER 5 rocket on April 9, 1992, a small spacecraft, the Ejectable Ballistometer (EB), was separated from the MASER payload. After separation, the EB continued on its own trajectory until impact with earth after 370 seconds. Two photographs of the launch of the EB are shown in figure 3.16. During its lifetime the EB performed a flat-spin manoeuvre (see also the previous section).

The EB consists of an experiment tank that contains approximately 2.7 kilograms of water, which is about 50% of the total volume of the tank. The experiment tank is an annular cylinder of which the inner and outer radius are equal to 0.125 m and 0.145 m respectively and the height is equal to 0.323 m. The dry mass of the EB is 18.8 kg and its moment-of-inertia tensor is a diagonal matrix diag $(0.25, 0.38, 0.37)$ kgm^2. Since the annular width of the tank is much smaller than the axial and azimuthal dimensions of the tank, the radial velocity of the liquid can be neglected with respect to the axial and azimuthal velocities. Also, the radius of curvature in the radial direction is much smaller than the radius of curvature in the axial and azimuthal directions. Hence, the free surface will deform in the axial and/or azimuthal directions mainly and the flow can be assumed

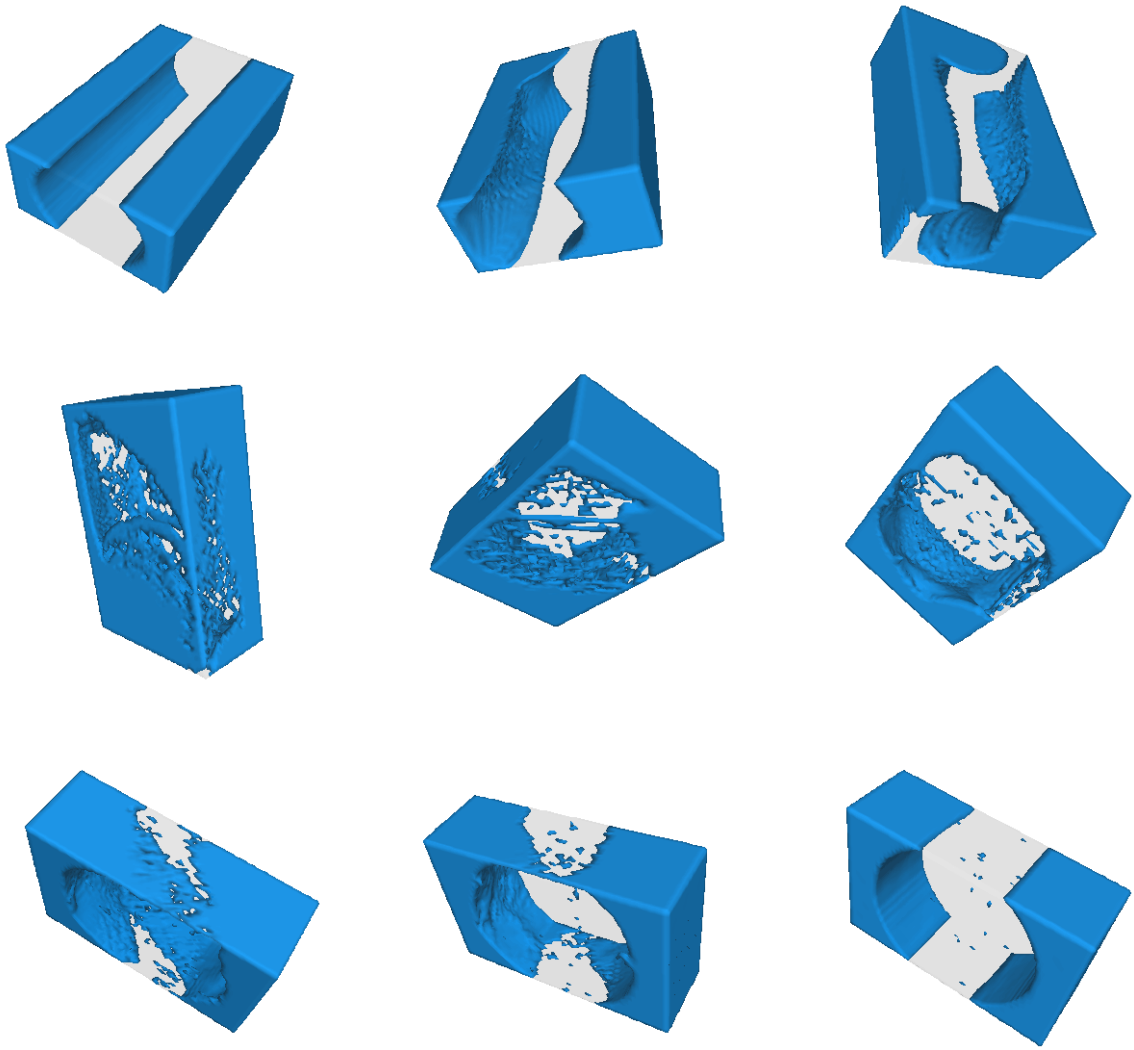

Figure 3.15: *Three-dimensional snapshots of the flat-spin simulation with a filling ratio of 40%.*

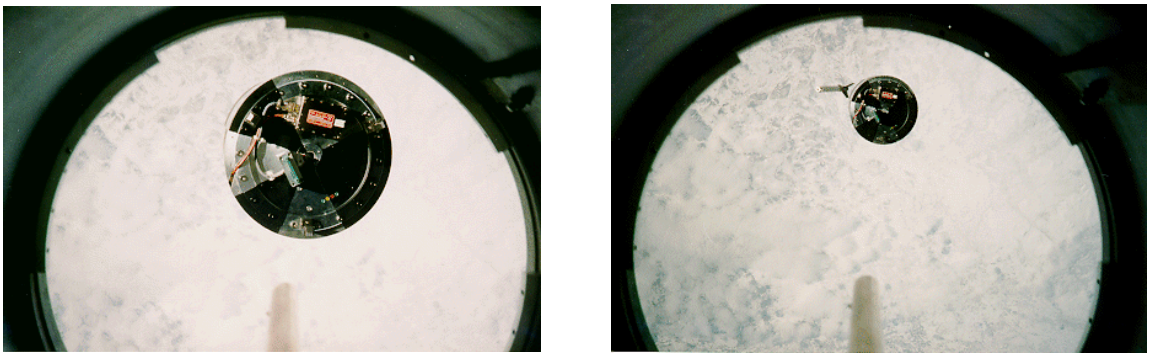

Figure 3.16: *Photographs of the separation from MASER of the Ejectable Ballistometer taken during the Wet Satellite Model experiment (these photographs were taken from http://www.nlr.nl/public/hosted-sites/mgcd/EXPMNT/A-015.html).*

to be two-dimensional. This simplification to a two-dimensional liquid-dynamics problem was an important feature of the WSM experiment since in 1992 no numerical models were known that could simulate a three-dimensional analogue of the WSM experiment.

When the EB was released from the MASER payload, its axis of symmetry was aligned with the direction of separation push. Hence, all the liquid inside the experiment tank was initially located in the bottom half of the tank. The initial motion of the EB was induced by transferring angular momentum from a flywheel. The flywheel axis was aligned with the axis of symmetry, *i.e.* the axis with minimum moment of inertia. Thus, the initial rotation of the EB was around this axis, whence a flat-spin transition could be expected. The amount of angular momentum transferred from the flywheel had been calibrated on ground, such that the initial angular velocity around the axis with minimum moment of inertia was known accurately.

A simulation of the WSM experiment has been performed with the method that has been presented in this thesis (although liquid sloshing has been studied in an EB-like geometry [85], ComFlo is the first method that simulates the WSM experiment). As in the experiment, the lower half of the annulus was filled with liquid and an initial angular velocity of 1.2 radians per second around the cylindrical axis was prescribed. For this simulation a grid consisting of $60 \times 60 \times 60$ cells was used and the time step, which was automatically adjusted based on the CFL number, varied from $\delta t = 2.5 \times 10^{-4}$ to $\delta t = 4 \times 10^{-3}$. The total simulation time was 370 seconds corresponding to the experiment time. Results from the simulation and the actual experiment are shown in figure 3.17.

Although the geometry of the EB is not very suitable for a method based on Cartesian grids — a cylindrical grid would be more appropriate —, the qualitative agreement between experiment and simulation is satisfactory. Indeed, the interval in which the angular velocity around the x-axis decreases from its initial value to zero is of the same order (approximately 200 seconds) in both the simulation and the experiment. Further, the frequencies of the oscillations in the angular velocities around the y- and z-axis in the simulation are comparable with those in the experiment. In particular the high-frequency oscillations in the first half and the low-frequency oscillations during the second half of the flat spin appear both in the experiment and the simulation. Also, the amplitude of the oscillations in the simulation is of the same magnitude as in the experiment. In the experiment, after about 200 seconds, the angular velocity around the y-axis is ap-

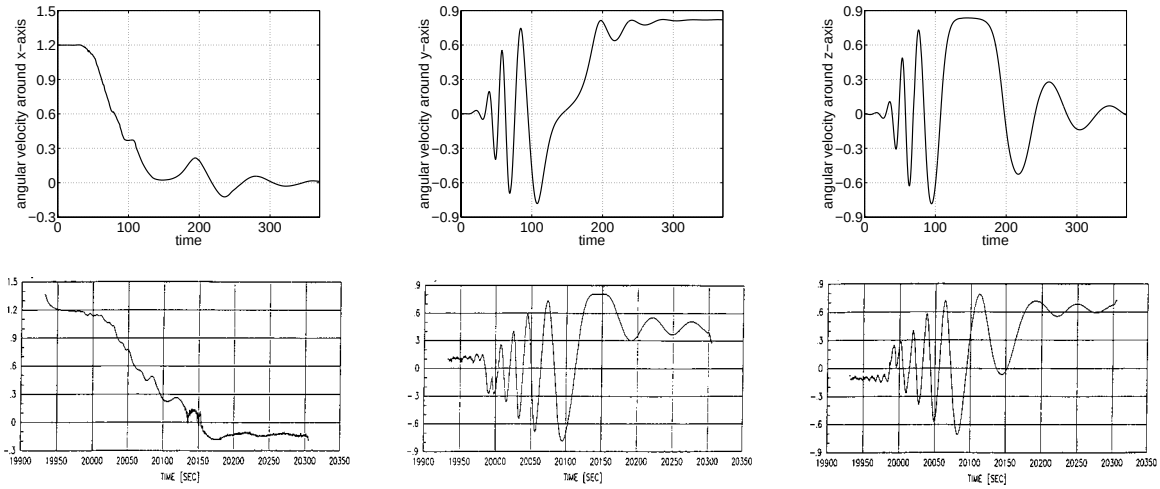

Figure 3.17: *Angular velocities around x- (left), y- (middle), and z-axis (right) in the Wet Satellite Model experiment. Comparison of simulation (top) to experiment (bottom). Note that the simulation time index 0 corresponds to an experiment time index of 19950 approximately.*

proximately constant for almost 40 seconds. This phenomenon is also present in the simulation, however, not in the angular velocity around the y-axis but around the z-axis and somewhat earlier than in the experiment.

In the simulation the angular velocity around the z-axis vanishes in the final stage of the flat spin. This behaviour is not visible in the experiment, where the EB seems to settle itself into a steady state in which it is rotating both around the y- and z-axis. Since the rotation axis in the steady state depends on the moment-of-inertia tensor of the coupled system and thus on the liquid distribution, apparently, the free-surface configuration that is predicted by the simulation does not agree with the experiment. Unfortunately, the free-surface configuration was not monitored during the WSM experiment. Hence, no further conclusions about this disagreement between simulation and experiment can be drawn.